



# Broadband optical detection of strain waves in a thin ruthenium film

T. J. VAN DEN HOOVEN,<sup>1,\*</sup>  L. CRUCIANI,<sup>1,2</sup>  AND P. C. M. PLANKEN<sup>1,2</sup> 

<sup>1</sup>*Advanced Research Center for Nanolithography (ARCNL), Science Park 106, 1098 XG Amsterdam, Netherlands*

<sup>2</sup>*Van der Waals-Zeeman Institute, Institute of Physics, University of Amsterdam, Science Park 904, 1098 XH Amsterdam, Netherlands*

\*[t.vdhooven@arcnl.nl](mailto:t.vdhooven@arcnl.nl)

**Abstract:** Optimizing the optical detection of ultrafast strain waves is essential for potential applications in semiconductor metrology. A crucial element in this is the wavelength-dependent optical response to these waves, which is, unfortunately, not known for many materials. Here, using an ultrafast spectrometer, we investigate the strain-wave-induced changes in reflectance of a 30 nm ruthenium layer at wavelengths ranging from 475 nm and 1000 nm. We find that the maximum detectable strain-wave frequency is inversely proportional to the optical penetration depth of the probe wavelength. Consequently, the spectrum peak of the reflectance change induced by the strain-wave shifts from 80 GHz to 300 GHz, as the probe wavelength decreases from 1000 nm to 560 nm, respectively. Surprisingly, certain strain-wave frequencies are not observed below the maximum detectable frequency for specific probe wavelengths. This emphasizes that there is no simple relation between detection wavelength and the strength of the optical response of the material to strain waves.

© 2025 Optica Publishing Group under the terms of the [Optica Open Access Publishing Agreement](#)

## 1. Introduction

Ruthenium is a relatively new material in the semiconductor industry. It is a candidate metal to replace copper as a material for interconnects, the ‘wires’ connecting different layers in semiconductor devices. Copper suffers from ‘graininess’, as these interconnects become narrower (<20 nm), which increases resistivity [1]. Ruthenium suffers less from this problem and has a lower resistivity on the nanoscale than copper [2–4]. Furthermore, ruthenium may also be used as a selective etch mask (hard mask) in semiconductor device manufacturing, to protect areas from being etched [5–7].

In both cases, a layer of ruthenium, tens of nanometres thick, has to be deposited onto the silicon wafer on which the semiconductor devices are fabricated, covering the wafer completely. Unfortunately, thick layers of ruthenium are nearly opaque for most wavelengths. This can make optical metrology in semiconductor device manufacturing, especially wafer alignment metrology, challenging. In alignment metrology, the position of the wafer is determined using several ‘alignment gratings’, just before exposure in a photolithography machine, whose position is determined with (sub)-nanometre accuracy via the diffraction of (visible) light [8].

It has been shown that such gratings, when buried underneath opaque layers, can still be optically detected with the help of ultrafast laser-induced strain waves [9,10]. These strain waves are generated by the absorption of a short laser pulse, and are subsequently reflected off the buried grating, forming a strain-wave copy of the grating that travels back up to the surface, where it can be optically detected. One of the main challenges here is the optical detection of the strain waves with a sufficiently high signal-to-noise ratio (SNR) in a limited amount of time. In general, increasing the SNR can be done by either decreasing noise or increasing signal. One method to increase the SNR in the optical detection of strain waves, is to probe with wavelengths

close to optical resonances [11–15]. These resonances, when affected by the strain wave, can increase the change in reflectance and diffraction induced by the strain wave.

Improving the optical response to strain waves starts with selecting the ‘proper’ probe wavelength, where the change in reflectance, induced by the strain wave, is largest. Although there is some research on the behaviour of ruthenium under femtosecond illumination [16–20], there is no study of the broadband optical response of ruthenium to ultrafast strain waves. The best way to determine the proper probe wavelength is through experiments, as the linear optical reflection spectrum is typically not a good predictor for the strength of the strain-wave-induced change in reflectance [13].

Here, we present results of experiments on the strain-wave-induced changes in reflectance, as a function of probe wavelength and pump-probe delay time, of an approximately 30 nm thick ruthenium layer on sapphire, in a wavelength range from 475 nm to 1000 nm. We find that the strain-wave-induced reflectance changes show a strong dependence on the optical probe wavelength. Not only the amplitude, but also the temporal shape of the induced reflectance changes varies with probe wavelength. For probe wavelengths shorter than 900 nm, we observe a train of strain-wave-induced changes in reflectance, spaced 10 ps apart. The changes in reflectance become shorter and sharper in time, for shorter probe wavelengths. This is also evident in the spectrum of the time-dependent reflectance changes induced by the first reflection of the strain wave, which contains higher frequencies when measured at shorter probe wavelengths. We find that the maximum detectable frequency as a function of probe wavelength, more or less corresponds to the time it takes for the strain wave to propagate over a distance that corresponds to the optical penetration depth. Lastly, we find that the spectrum contains some gaps, most notably at a probe wavelength of 600 nm, where the strain-wave frequencies below 150 GHz are only very weakly present. This shows that the wavelength-dependent optical response to strain waves is not merely a function of penetration depth.

## 2. Methods

An amplified laser system (Astrella, Coherent) generates a 1 kHz pulse train consisting of 35 fs, 6 mJ pulses with a central wavelength of 800 nm. This pulse train is split into two beams by an 85 : 15 (R:T) beam splitter.

The weaker part is frequency-doubled using a  $\beta$ -barium borate (BBO) crystal, to a central wavelength of 400 nm, and is used to pump the sample. Every other pump pulse is blocked by an optical chopper, synchronized to the pulse train, such that the repetition rate is reduced to 500 Hz. A mechanical delay line (M-521.D, Physik Instrumente) varies the optical path length of the pump pulse. The pump pulse polarization is vertical with respect to the laser table and is weakly focussed onto the sample. The full-width at half maximum (FWHM) axes of the elliptic spot are 400  $\mu\text{m}$  and 500  $\mu\text{m}$ . The pump peak fluence is 9.4  $\text{mJ cm}^{-2}$ .

The stronger part, reflected by the beam splitter, pumps a three-stage optical parametric amplifier (OPA) (TOPAS-HE, Light-Conversion). About 1  $\mu\text{J}$  to 2  $\mu\text{J}$  of the OPA’s signal pulse, tuned to 1200 nm, is used to generate a white light continuum (WLC) in either a barium fluoride ( $\text{BaF}_2$ ) or a sapphire crystal. Barium fluoride is used for wavelengths between 470 nm and 760 nm [21]. For the longer-wavelength measurements, a sapphire crystal was used to generate the WLC probe pulse. For this wavelength range, using sapphire results in less pulse-to-pulse fluctuations in both spectral shape and total intensity, compared to  $\text{BaF}_2$ . After the generation crystal, the WLC pulse is collimated and focussed onto the sample, with an angle of incidence of about  $25^\circ$  with respect to the surface normal. The pulse is horizontally polarized, i.e., in the plane formed by the surface normal of the sample and the propagation direction of the probe pulse. The FWHM spot size of the probe pulse on the sample is approximately circular with a diameter of about 45  $\mu\text{m}$ , significantly smaller than the pump pulse spot size.

After the sample, the reflected probe pulse is collimated and measured by the spectrometer. The spectrometer consists of a grating with 300 lines per mm and a lens system, comprising two cylindrical lenses, with an effective focal distance of 75 mm that focusses the dispersed pulse onto a camera (Andor Zyla 4.2 Plus, Oxford Instruments). A reference measurement of the WLC is recorded by the same spectrometer, but at a different active area on the camera. For this, part of the WLC pulse is split off using a beam splitter, before it probes the sample. More details can be found elsewhere [13].

When the crystal that is used to generate the WLC is changed, the spectrometer grating is rotated to ensure that the wavelength range of interest is captured by the camera. Also, the beam splitter that splits the reference from the probe beam is swapped, and the spectrometer is calibrated again. Table 1 lists the wavelength ranges and the configurations that are used.

**Table 1. Configuration of the experimental setup for the different wavelength ranges.**

Wavelength range	WLC crystal (thickness)	Beam splitter (R:T)
470 nm to 760 nm	BaF <sub>2</sub> (2 mm)	Thorlabs BST10 (70:30)
730 nm to 1000 nm	Sapphire (5 mm)	Thorlabs UFBS8020 (80:20)

The ruthenium film was deposited onto a sapphire substrate, via magnetron sputtering at an argon plasma pressure of  $2 \times 10^{-3}$  mbar, with a rate of approximately  $0.25 \text{ nm s}^{-1}$ . The substrate was chemically cleaned using a solution of ammonium hydroxide (NH<sub>4</sub>OH) and hydrogen peroxide in water, and subsequently rinsed in isopropanol and dried using N<sub>2</sub> gas.

### 3. Results

Ruthenium has a strong electron-phonon coupling constant [22,23], which means that most of the pump pulse energy, initially absorbed by the free electron gas, is transferred to the lattice within the first picosecond after illumination with the pump pulse. We present, and briefly discuss, the pump-induced changes in reflectance during the first few picoseconds after illumination in Appendix A. The rapid transfer of energy to the lattice results in, (i) limited initial energy diffusion deeper into the layer, as most of the energy is deposited close to the surface as a result of the short penetration depth of the pump light and, (ii) the generation of very-high-frequency strain waves at the surface and back interface of the layer. The amplitude of the strain wave generated at the front surface is much larger than that of the strain wave generated at the back interface due to the short penetration depth of the 400 nm pump wavelength and the limited energy diffusion in the electron gas during the first few picoseconds.

In Fig. 1(a), we show the measured relative changes in reflectance, averaged over a 2.1 nm optical bandwidth, as a function of pump-probe delay, at probe wavelengths of 500 nm, 700 nm, and 900 nm. The measurements are shifted in time such that the onset of the initial changes is at 0 ps, for all measurements. The reflectance for 700 nm and 900 nm increases abruptly at 0 ps pump-probe delay time, while the reflectance at 500 nm abruptly decreases and also recovers quickly. These initial changes are mostly related to electron dynamics and are discussed in Appendix A. After the rapid increase, the reflectance at 700 nm and 900 nm decays exponentially, on a timescale of about 30 ps, from values of about 2% and 4.2%, to 1.2% and 3%, respectively. This decay is the result of the redistribution of energy *within* the ruthenium layer from near the surface, where most of the energy is initially deposited, deeper into the layer. The reflectance at 500 nm is, however, mostly constant in time, at a level slightly lower than its static reflectance. Furthermore, the exponential decay appears to be absent.

Centred at approximately 11 ps, all three wavelengths show a rapid change in reflectance. This is shown in more detail in Fig. 1(b), where the slowly-varying background is removed. The strain-wave spectra are shown in sub-figure c. For 900 nm, the change is a decrease in reflectance lasting a few picoseconds, superimposed on the exponential decay. For 700 nm, the change is

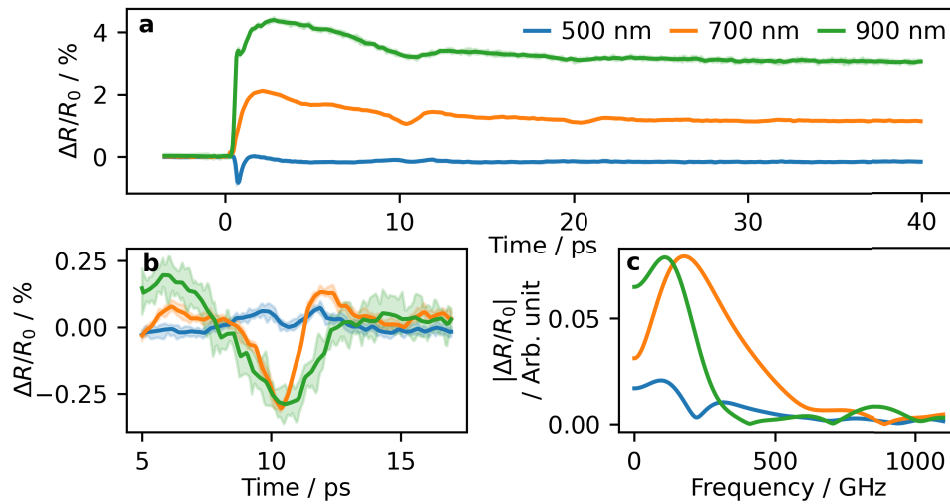


**Fig. 1.** a. Changes in reflectance of a 30 nm ruthenium film as a function of delay between the 400 nm pump pulse and the probe pulse, for three probe wavelengths of 500 nm, 700 nm and 900 nm. b. Background-removed strain-wave-induced reflectance changes for the three wavelengths, centred at 11 ps. c. Strain-wave spectrum of the three strain-wave-induced changes in reflection, shown in b.

more bipolar: first a decrease in reflectance, followed by an increase, relative to the exponential decay. At 500 nm, the change consists of two small increases in the reflectance, with a dip in the middle. These rapid changes are induced by a strain wave, generated by the thermal expansion of the hot lattice, returning to the surface, where it was generated, after being (partially) reflected at the back interface of the ruthenium layer and the sapphire substrate.

A similar rapid change in reflectance is visible at a pump-probe delay time of 21 ps for probe wavelengths of 700 nm and 900 nm. These changes are again caused by the strain wave as it has completed its second round trip. The amplitude of the changes is smaller, as the strain wave is, again, only partially reflected at the back interface. From the roundtrip time of 10.0 ps and the speed of sound of ruthenium of  $5970 \text{ m s}^{-1}$  [24], we calculate a layer thickness of 29.9 nm, close to the value of the intended 30 nm thickness.

To investigate the probe-wavelength-dependence of the strain-wave-induced changes in reflectance, we remove the thermal background by fitting an exponential decay to the change in reflectance for every measured probe wavelength. In Fig. 2(a) and (b), we plot the strain-wave-induced changes in reflectance as a function of time (horizontal axis) and as a function of probe wavelength (vertical axis), obtained from the long-wavelength interval measurement (a) and the short-wavelength interval measurement (b). A decrease in reflectance is indicated by the colour blue, white indicates little or no change, and red indicates an increase in reflectance. The amplitudes shown in panel a (and c) are multiplied by a factor of 1.36 to account for an apparent difference in pump fluence, see Appendix D for more information.

In Fig. 2(a) and (b), we again observe the first reflection of the strain wave at around 11 ps. For a probe wavelength of 1000 nm, the strain wave induces a decrease in reflectance, lasting about 4 ps, centred at 11 ps. The duration of this decrease in reflectance gradually becomes shorter for shorter probe wavelengths. At 760 nm, the shortest wavelength shown in panel a, the strain-wave-induced decrease in reflectance only lasts about 2 ps. For the shorter probe wavelengths shown in panel b, this trend continues: the induced change in reflectance becomes sharper and shorter for shorter wavelengths. In addition to this, the strain-wave-induced change in reflectance becomes gradually asymmetric for probe wavelengths shorter than 860 nm. The

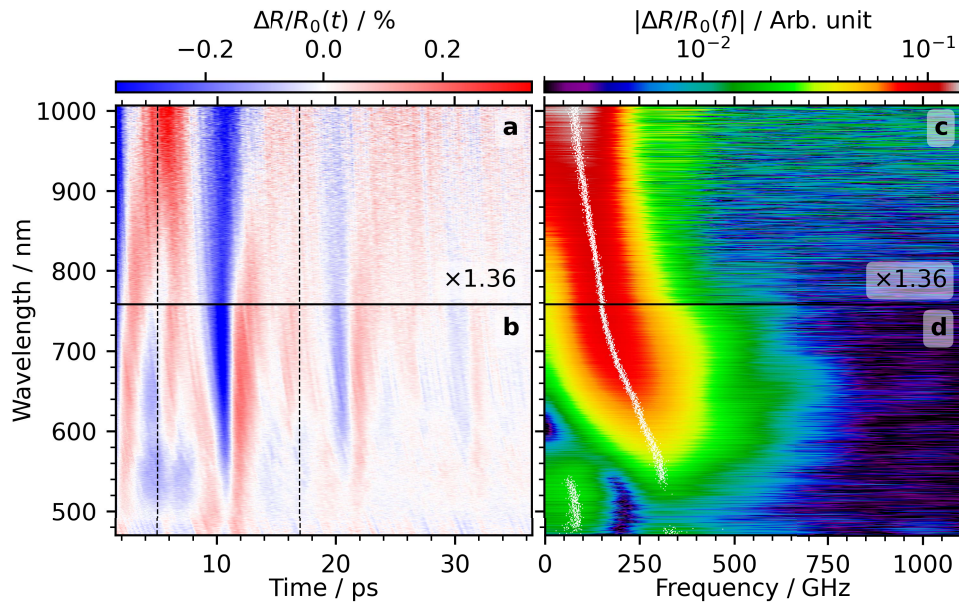


**Fig. 2.** a and b: Measured strain-wave-induced changes in reflectance of a 30 nm thick layer of ruthenium on sapphire, after removing the thermal background. c and d: FFT amplitudes of a time interval around the first strain-wave-induced change in reflectance, at 11 ps, shown in a and b. This interval, from 5 ps to 17 ps, is indicated by the vertical black dashed lines in a and b. The white dots indicate the frequency with the highest amplitude for every wavelength. The amplitudes in a and c are multiplied by a factor of 1.36, see Appendix D.

reflectance change is almost bipolar between 750 nm and 620 nm. For probe wavelengths short than 620 nm, an increase in reflectance is observed before the rapid decrease centred at 11 ps. Furthermore, the amplitude of this change at 11 ps also decreases for shorter probe wavelengths. At 500 nm, the change in reflectance only consists of two positive peaks, at about 9.5 ps and 12 ps. Between the shoulders, the reflectance decreases a little, this can be seen best in Fig. 1, for the probe wavelength of 500 nm.

We use a fast Fourier transform (FFT) algorithm to calculate the Fourier transform of the time-dependent change in reflectance in an interval centred at 11 ps, the middle of the strain-wave-induced change in reflectance, for all probe wavelengths. This interval starts at 5 ps and ends at 17 ps, is shown with two dashed vertical lines in Fig. 2. A Hann window is used to reduce windowing effects in the Fourier transform.

Figure 2(c) and (d) show the amplitude of the Fourier transform, as a function of frequency (horizontal axis), and of probe wavelength (vertical axis). The amplitude is plotted in a logarithmic colour scale, shown above the plot. For every probe wavelength, the frequency with the highest amplitude is indicated with a white dot. At a probe wavelength of 1000 nm, the spectrum of the strain-wave-induced change in reflectance peaks at approximately 80 GHz and extends to 400 GHz. As the probe wavelength decreases, the peak of the spectrum shifts to higher frequencies. At 760 nm, at the intersection between the two sets of measurements, the calculated spectrum peaks at 150 GHz. Between 590 nm and 700 nm, the highest frequencies contained in the high-frequency tail even approach 800 GHz. It is important to note that these changes are correlated with the probe wavelength, as the strain wave probed by every wavelength is always the same.

The *peak* of the spectrum reaches its highest frequency of 300 GHz around 560 nm. However, the maximum spectral amplitude starts decreasing for probe wavelengths shorter than 650 nm,

corresponding to smaller strain-wave-induced changes in reflectance. Surprisingly, there are several gaps in the strain-wave spectrum for these shorter wavelengths. The first gap is at the lowest frequencies, below 150 GHz, for probe wavelengths between 590 nm and 620 nm. The second gap is present at 200 GHz, for wavelengths shorter than 540 nm. This shows that there is not a simple relation between optical probe wavelength and the magnitude of the strain-wave-induced changes in reflectance.

Finally, we note that the noise floor at the longer probe wavelengths, especially in panel c of Fig. 2, is higher than for the shorter wavelengths. This is mainly due to the low quantum efficiency of the silicon complementary metal-oxide semiconductor (CMOS) camera used in the spectrometer, which results in a lower SNR for the longer wavelengths.

The Fourier transform of the full time interval is shown in Fig. 9. It contains the same frequencies, but the spectrum is now modulated at 100 GHz, due to the second and third reflections of the strain wave that arrive at 10 ps intervals.

#### 4. Discussion

The maximum optically detectable strain-wave frequency is, according to [25], given by either the Brillouin frequency or by a frequency inversely proportional to the penetration depth of the probe wavelength. We will first discuss the Brillouin oscillation and frequency.

We assume an infinitely short, plane strain wave propagating in a transparent, isotropic material, with a (real) refractive index  $n$ . A probe pulse, with wavelength  $\lambda_0$ , is (at normal incidence) incident on the strain wave and is partially reflected. The reflected field is constant, if the strain wave does not change while it propagates. A detector, only sensitive to the intensity of the reflected probe pulse, then measures a signal constant in time. However, typically we measure a strain wave in a *layer*, where the surface also reflects part of the light. The probe reflection from the surface interferes with the probe reflection from the strain wave and changes the measured intensity. Since the strain wave moves at the speed of sound,  $v_s$ , in the material, the path length of the probe's reflection off the strain wave changes too, with twice the speed of sound, as the probe has to travel to and from the strain wave. When the path length difference equals an integer multiple of the wavelength of the probe light in the material,  $\lambda_0/n$ , the phase of the probe's reflection is the same, and the reflections constructively interfere. The time it takes for the intensity to complete one period of oscillation, the Brillouin oscillation period, is then given by  $t_B = \lambda_0/(2nv_s)$ . This also implies that the Brillouin oscillation frequency,  $f_B = 2nv_s/\lambda_0$ , is the *only* frequency that is measured, and is independent of the shape of the strain wave. This mechanism is commonly referred to as time-domain Brillouin scattering, and its relation to frequency-domain Brillouin scattering is discussed in [26].

Now, consider a material that strongly absorbs, and in which light has a finite penetration depth. In this case, we can only measure the strain wave if it is inside the optical penetration depth at the probe wavelength,  $\delta_p$  in the material. Furthermore, the distance of the strain wave to the surface not only influences the phase of the field reflected from the strain wave, but also the *amplitude* of this field. Again, we consider an infinitely short strain wave. Assuming a relatively long penetration depth, this very-high-frequency strain wave will result in a change in reflectance that is 'smeared' out in time. In contrast, a probe pulse with a short penetration depth only measures the strain wave if it is very close to the surface, resulting in a short time when the reflectance is affected by the strain wave. So, the time it takes for the infinitely short strain wave to propagate through this volume determines the maximum frequency with which we can detect the strain wave. This frequency is then proportional to  $f_p = v_s/\delta_p$  [25].

Time-domain Brillouin oscillations observed in reflectance with frequency  $f_B$  are caused by interference between light reflected off the propagating strain wave and light reflected off the (front) surface. As the strain wave propagates, the optical path length difference between the two reflected beams changes, creating a contribution to the time-dependent reflectance, that oscillates

with optical path length difference. If we can ignore time-domain Brillouin oscillations as described above (as we will argue later), the only time-dependent changes in probe reflectance are caused by the strain wave periodically entering the region corresponding to the probe penetration depth. The time between the periodic features observed in the reflectance measurements, is then the round trip time of the strain wave in the medium. The spectrum of each individual rapid change is thus limited by  $f_p$ .

In Fig. 3, we plot the amplitude of the Fourier transform of the first strain-wave-induced change in reflectance as a function of probe wavelength and frequency, similar to Fig. 2(c) and (d), but mirrored and rotated. For each optical probe wavelength, we have normalized the spectrum to the maximum amplitude of that probe wavelength. As a result, we can more easily compare the differences in the strain-wave spectra measured at different probe wavelengths. The spectra are smoothed by applying a moving average over 10 spectra in the horizontal direction. On top of these spectra, the Brillouin frequency,  $f_B$ , and the frequency associated with the penetration depth,  $f_p$ , are plotted as a function of probe wavelength, in black and red, respectively. These are calculated using the complex refractive index,  $\tilde{n}$ , given by [27] and the speed of sound,  $v_s = 5970 \text{ m s}^{-1}$ , taken from [24]. For simplicity, the frequencies are calculated assuming normal incidence of the probe beam. The actual angle of incidence of  $25^\circ$  is expected to have ultimately little effect, due to strong refraction towards the surface normal, as the (complex) refractive index of ruthenium is high ( $>3.5$ ) [27] in the wavelength range considered. The small effect by assuming perpendicular incidence on the sample on the frequencies is therefore neglected to simplify the calculations.

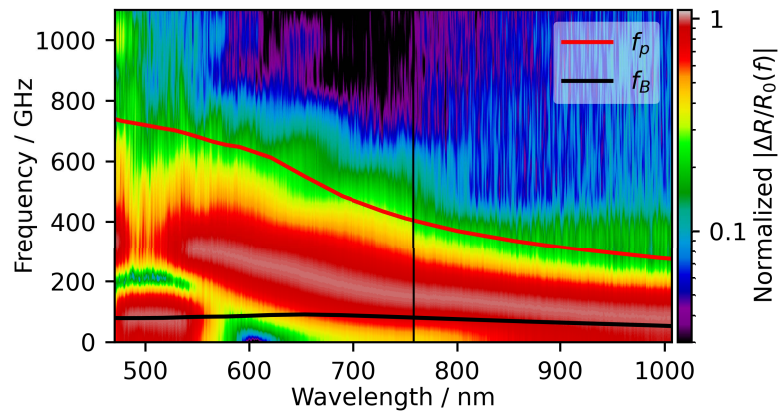


**Fig. 3.** Strain-wave amplitude, normalized to the maximum amplitude for every wavelength, as a function of frequency (vertical) and wavelength (horizontal). The spectra are smoothed in the horizontal direction by a moving average over 10 spectra. The Brillouin frequency,  $f_B$ , (black line) and the frequency associated with the penetration depth,  $f_p$ , (red line) are calculated using the refractive index of ruthenium taken from [27].

We check the strain wave frequency spectrum by calculating the position-dependent displacement (and the strain) in the layer via the elastic wave equation (Eq. (1)). The spectrum of the strain wave extends well above 1 THz, as can be seen in Fig. 8 in Appendix B. Especially for the positions close to the surface, the amplitude at 1 THz is still about half of its peak amplitude at approximately 300 GHz.

As can be seen,  $f_p$  coincides with the frequencies at approximately 20% of the peak amplitude and reflects the wavelength dependence observed in the measured frequency spectrum. We note that  $f_p$  is calculated with literature values for the refractive index and speed of sound in ruthenium.

In contrast, the Brillouin oscillation frequency is well below the frequencies where the amplitude peaks, and is not strongly wavelength dependent. The frequency is about 53 GHz at 1000 nm, peaks at approximately 650 nm with 90 GHz, and decreases to about 78 GHz at 470 nm. The decrease in  $f_B$  for wavelengths shorter than 650 nm is due to a decrease in the real part of the complex refractive index of ruthenium for those wavelengths. That the calculated Brillouin frequency is well below the frequencies where the amplitude peaks, is not unexpected, as the time-dependent Brillouin oscillations are caused by changes in the interference between light reflected at the surface, and light reflected from the propagating strain wave. To observe these oscillations, the phase difference between the two optical waves must be large enough and change over at least  $\pi$  as the strain wave propagates through the layer. However, due to the short optical penetration depth in ruthenium and due to the layer thickness of only 30 nm, this does not occur. Brillouin oscillations are thus not observed.

We would like to point out that the largest strain-wave-induced changes in reflectance are *not* necessarily measured at the shortest probe wavelengths. For example, in Fig. 2(d), it seems that the highest frequencies are observed between 600 nm and 700 nm, but this mainly caused by the larger amplitude of the strain-wave-induced changes in reflection at those wavelengths, compared to those at the shortest wavelengths. Note that  $f_B$  and  $f_p$  do not take the (probe-wavelength-dependent) ‘strain-optic’ coefficient,  $\partial\tilde{n}/\partial\eta$ , into account, where  $\eta$  is the strain.

Probing with a wavelength that has a larger penetration depth may result in a larger strain-wave-induced change in reflectance, as the strain-wave amplitude goes to zero near a free surface. This is the result of the stress-free boundary condition at such a surface. From the elastic equations [20], we have

$$\sigma_z = (\lambda + 2\mu)\eta_z - \sigma_{\text{thermal}}, \quad (1)$$

where  $\sigma_z$  is the stress in the  $z$ -direction, perpendicular to the interface,  $\lambda$  and  $\mu$  are the first and second Lamé parameters, that determine the relation between stress and strain in materials,  $\eta_z$  is the strain, and  $\sigma_{\text{thermal}}$  is the thermal stress in the material. A free surface is free to move and the stress on this surface is zero. Hence, the strain is proportional to the slowly varying thermal stress. The strain-wave amplitude therefore is zero at the interface, and still small close to the interface. This can also be seen in Fig. 8 in Appendix B, where the strain wave amplitude close to the surface is very small. Another consequence of this boundary condition is that the wave is perfectly reflected at the interface.

A larger penetration depth thus allows one to probe where the strain-wave amplitude is larger. A different approach to this problem is to add a transparent layer to the surface, and thereby changing the boundary conditions. Now, the surface where the strain wave amplitude is zero is the surface of the transparent layer and the strain-wave amplitude at the transparent layer/metal interface is no longer zero. This can result in probing a strain wave with a larger amplitude, close to the surface of the absorbing layer, as is demonstrated in [28].

Finally, there are some gaps in the spectrum, which are visible in Fig. 3 at, for example, the low frequencies for probe wavelengths around 600 nm or the frequencies around 200 GHz for probe wavelengths between 480 nm and 550 nm. Furthermore, we find that the vanishing of the amplitude of the low strain-wave frequencies around a probe wavelength of 600 nm is accompanied by a phase shift of the low-frequency components, when comparing the phase of these frequencies for probe wavelengths above and below 600 nm. In Fig. 4(a) and (b), we plot the high-pass and low-pass filtered changes in reflectance as function of time (horizontal) and probe wavelength (vertical), for the short-wavelength set of measurements. The changes are plotted in a linear colour scale, that is shown next to panels a and b. An 8<sup>th</sup>-order, zero-phase, digital filter is used, with cut-on (Fig. 4(a)) and cut-off (Fig. 4(b)) frequencies of 150 GHz, which is in the gap between the first and second peak of the spectrum, as seen in Fig. 9 in Appendix C. In panel a, the high-pass filtered changes are becoming sharper for the shorter probe wavelengths, since higher strain-wave frequencies are detected. However, in panel b, the phase of the (slow)

oscillation changes at a probe wavelength around 600 nm. This is indicated by the slanted black dashed lines, which follow the peaks and valleys of the low-frequency oscillatory change in reflectance.

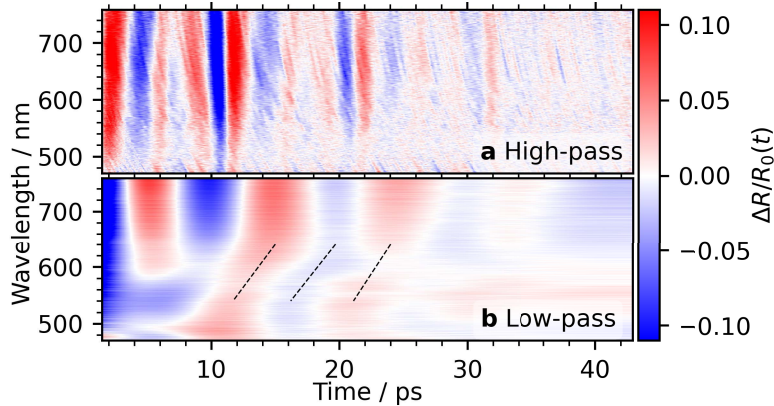


**Fig. 4.** a. High-pass filtered (cut-on frequency: 150 GHz) strain-wave-induced changes in reflectance for the short-wavelength set of measurements. b. Low-pass filtered (cut-off frequency: 150 GHz) strain-wave-induced changes. The black dashed lines show the change in the phase of the low-frequency oscillations around 600 nm.

We speculate that both the vanishing amplitude and the change in phase for certain strain-wave frequencies may be related to what is described in [29]. In that article, the authors describe the relation between the measured strain-wave-induced changes in reflectance as a function of strain-wave frequency and the strain wave with a frequency-dependent transfer function. This transfer function depends on the wave number of the optical probe, wave number of the strain wave in the medium, the dielectric function of the medium and its derivative with respect to strain. In their description, the transfer function, for all strain-wave frequencies, is always a purely imaginary number. So, for a fixed probe wavelength, the transfer function, for increasing strain-wave frequency, is allowed to cross zero and continue on the other side of the imaginary axis. This would result in a  $\pi$ -phase shift for the higher frequencies, for which the transfer function amplitude is larger than zero. Conversely, the same may happen when the probe wavelength is varied, for a fixed strain-wave frequency. It appears, however, that the phase shift of the low-frequency components of the reflectance change around 600 nm, indicated by the black dashed lines in Fig. 4(b), is not exactly  $\pi$ . This could be due to the low amplitude of the reflectance changes for the shortest wavelengths, as this makes accurately determining the phase more difficult.

## 5. Conclusions

We have measured the ultrafast strain-wave-induced changes in reflectance of a 30 nm ruthenium layer on a sapphire substrate, as a function pump-probe delay time and probe wavelength. Two sets of measurements were conducted, one for wavelengths between 480 nm and 760 nm, the other for wavelengths between 730 nm and 1000 nm. For all probe wavelengths, we detect strain-wave-induced changes in reflectance, with a period of 10 ps. But for wavelengths shorter than 900 nm, a train of isolated strain-wave-induced changes in reflectance is measured, spaced 10 ps apart. These individual pulses contain frequencies up to 800 GHz, when detected at optical wavelengths around 650 nm. However, the amplitude of the changes in reflectance decreases for wavelengths shorter than 600 nm. Furthermore, we find that the maximum detectable frequency, as a function of probe wavelength, corresponds to the time it takes for the strain

wave to propagate through the optical penetration depth at that probe wavelength. Finally, we observe some frequency components that have a very low amplitude. Most notably, almost no strain-wave-induced change in reflectance is measured for strain-wave frequencies below 150 GHz for probe wavelengths around 600 nm. This absence of signal is accompanied by a phase shift, when we compare the low-frequency changes in the reflectance at probe wavelengths above and below the probe wavelength of 600 nm. This clearly shows that the wavelength-dependence of the strain-wave-induced change in optical reflectance is not a simple function of penetration depth of the probe wavelength.

### A. Electron dynamics

Ultrafast strain waves are generated by the rapid expansion of the ruthenium layer due to heating of the metal lattice after illumination with the pump pulse. The pump pulse energy is initially absorbed by the free electron gas and is transferred to the lattice via electron-phonon coupling. In this section, we probe the reflectance during the first few picoseconds after illumination, where the electron dynamics are expected to be strongest.

We plot the pump-induced changes in reflectance as a function of pump-probe delay, for four probe wavelengths, 480 nm, 580 nm, 650 nm, and 730 nm in Fig. 5(a). The measured changes in reflectance are shifted in time such that the onset of the changes is approximately the same, i.e., the chirp in the white light probe pulse has been corrected afterwards.

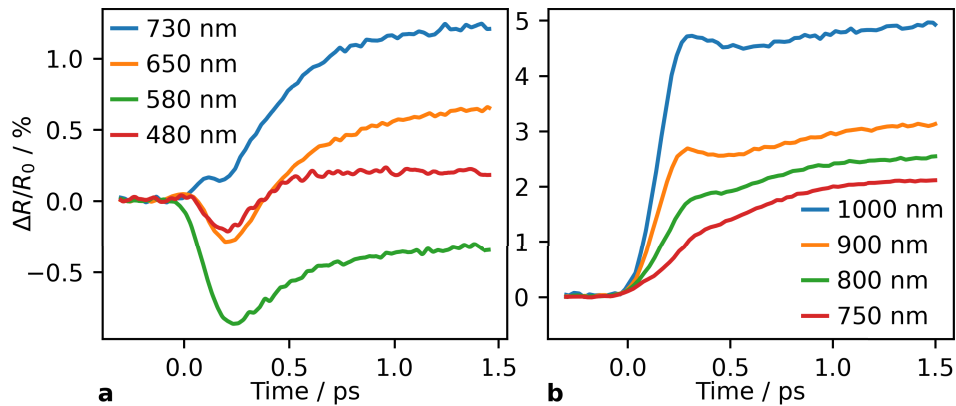


**Fig. 5.** a. Measured changes in reflection of the 30 nm ruthenium layer as a function of pump-probe delay, for probe wavelengths of 730 nm, 650 nm, 580 nm and 480 nm. b. Same for probe wavelengths of 1000 nm, 900 nm, 800 nm and 750 nm, which were obtained in a separate measurement.

The reflectance of the shortest probe wavelength shown, 480 nm, initially decreases and reaches a minimum of about 0.2% lower than its static reflectance at about 200 fs. After that, the change in reflectance becomes positive and reaches a constant value of 0.1% at 500 fs. At 580 nm, the change in reflectance also reaches a minimum at 200 fs, at -0.7%. It recovers slightly, but the change remains negative at about -0.4% after the minimum. At 650 nm, the reflectance shown a similar change as at 480 nm, although the change in reflectance is about 0.5% after 1 ps. The change in reflectance at 730 nm is strictly positive. However, at 200 fs, the change shows a ‘wobble’, before increasing to its maximum value of 1.2% at 1 ps.

In Fig. 5(b), the changes in reflectance as a function of pump-probe delay, of four longer probe wavelengths, of 750 nm, 800 nm, 900 nm, and 1000 nm, are plotted. The reflectance at 750 nm increases gradually, until it reaches a level about 2% higher than the static reflectance. The reflectance for the longest wavelengths, 800 nm, 900 nm, and 1000 nm increases more abruptly

and almost like a step-function when the ruthenium is illuminated by the pump pulse. The reflectance reaches a constant level of 2.2 %, 2.8 %, and 4.7 % for wavelengths of 800 nm, 900 nm, and 1000 nm, respectively.

The wavelengths, shown in Fig. 5(a), have been selected as they are representative of four regimes observed in the full measurement, which is shown in Fig. 6(a). Here, the changes in reflectance, as a function of pump-probe delay (horizontal axis) and probe wavelength (vertical axis), are shown in a colour scale. Red indicates an increase in reflectance, blue a decrease in reflectance and white indicates little or no change. Also, the chirp of the WLC pulse has been corrected by fitting a fifth-order polynomial to the onset of the change for each probe wavelength. This onset is defined as the first point to cross the threshold of 5 % of the maximum amplitude of the change in reflectance for that probe wavelength. The first regime, represented by 480 nm, contains the shortest probe wavelengths up to 490 nm and shows, initially, a decrease in reflectance. After the initial decrease, the reflectance for these wavelengths recovers to a slight increase. The second regime contains wavelengths between 490 nm and 630 nm, which show a strictly negative change in reflectance. The third regime contains wavelengths between 630 nm and 690 nm that show a similar change in reflectance as the first regime, initially negative but later positive. The change in reflectance of wavelengths longer than 690 nm, in the fourth regime, is only positive. Also, the longer wavelengths shown in Fig. 6(b) belong to this regime.

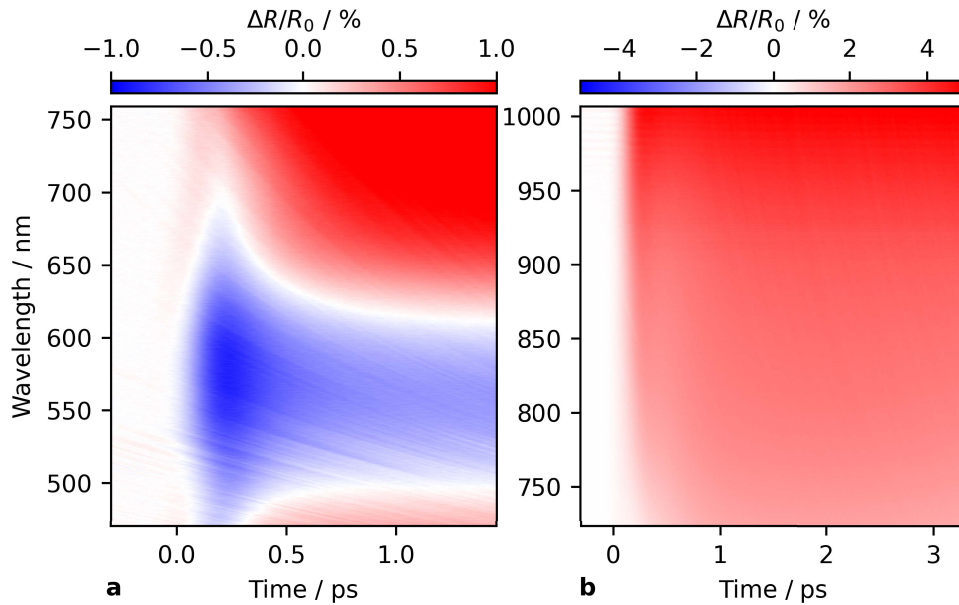


**Fig. 6.** Changes in reflectance as a function of probe wavelength and pump-probe delay time. The chirp has been removed. Panel a shows the short-wavelength measurement, panel b the long-wavelength measurement.

The evolution of the temperature in metals, shortly after illumination by an intense fs pulse, is often described by the two-temperature model (TTM) [30]. In this model, the free electron gas and the metal crystal lattice are treated as separate but coupled thermodynamic systems, each with its own temperature,  $T_e$  and  $T_l$ , respectively. The laser energy is absorbed by the electron gas and transferred to the lattice via electron-phonon scattering. The TTM, in one dimension, can be written as a function of two coupled heat equations as [30]:

$$C_e(T_e) \frac{\partial T_e}{\partial t} = \frac{\partial}{\partial z} \left( \kappa_e(T_e, T_l) \frac{\partial T_e}{\partial z} \right) - G(T_e - T_l) + S(z, t), \quad (2)$$

$$C_l \frac{\partial T_l}{\partial t} = G(T_e - T_l). \quad (3)$$

Here,  $C_e$  and  $C_l$  are the heat capacities of the electron gas and lattice, respectively,  $\kappa_e$  is the electron thermal conductivity,  $G$  is the electron-phonon coupling constant and  $S(z, t)$  is the absorbed laser energy density.

This system is solved numerically, using a forward difference method. The layer is treated as free-standing and Neumann boundary conditions (no heat flux through the boundaries) are used. The electron heat capacity as a function of electron gas temperature and the electron thermal conductivity as function of electron gas and lattice temperatures are taken from [23]. The electron-phonon coupling constant  $G = 1.85 \times 10^{18} \text{ W m}^{-3} \text{ K}^{-1}$  is taken from [31], and the lattice heat capacity is  $2.95 \times 10^6 \text{ J m}^{-3} \text{ K}^{-1}$  [20]. By multiplying the absorption profile as a function of depth with a Gaussian intensity distribution in time, the absorbed pump laser energy is calculated. The absorption profile is calculated with the transfer-matrix method (TMM) python package [32] for a 30 nm ruthenium thin film on a sapphire substrate. The  $n, k$  values of Ru are obtained via ellipsometry of a Ru layer deposited using the same process as is used here. The Gaussian intensity distribution has a FWHM pulse length of 60 fs, peaks at 250 fs, and has a (peak) fluence of  $9.4 \text{ mJ cm}^{-2}$ , matching the experimental parameters.

Figure 7(a) shows the calculated electron gas and lattice temperature at the surface of the Ru layer, as a function of time. The electron temperature at the surface peaks at 290 fs, only 40 fs after the peak of the laser pulse, at 2770 K. After this, the electron temperature decreases rapidly as energy is transferred to the lattice, as the electron-phonon coupling in Ru is very strong. As a result, the lattice temperature increases by almost 400 K in the 500 fs after the peak of the laser pulse. At the surface, the lattice and electron gas are in *local* thermal equilibrium after 920 fs, at a temperature of 630 K. The deposited energy is still mainly concentrated near the surface, where most of the pulse energy is absorbed. From this moment on, the energy will be distributed evenly throughout the layer, by the electron gas, as the lattice itself does not conduct heat in this formulation of the TTM (see Eq. (3)). As a result, the electron gas temperature is higher than the lattice temperature, near the back interface of the layer, while it is lower than the lattice temperature near the surface of the layer. This can be seen in Fig. 7(b), where the electron gas and lattice temperatures as a function of depth are plotted, at 289 fs and 920 fs. At the surface, the electron gas and lattice temperatures are in equilibrium, but deeper in the layer the electron temperature is still higher.

When comparing the electron and lattice temperatures at the surface, shown in Fig. 7, with the measured changes in reflectance, shown in Figs. 5, it is remarkable that, for wavelengths longer than  $\sim 700 \text{ nm}$ , the drastic increase in electron temperature is not evident from the change in reflectance. For the shorter wavelengths, this typical ‘electron’ peak in the reflectance appears to be present. This seems to be in agreement with results from the XUV Optics group at the University of Twente [16].

Finally, the lattice temperature distribution within the layer, as a function of time, also determines how the strain waves are generated. As soon as the lattice temperature starts to increase, the lattice starts to expand. Only the surface and the interface with the substrate are free to move, hence that is where strain waves will be generated. The lattice temperature from the surface increases from its initial temperature of 300 K to almost 700 K in about 500 fs. The surface will thus rapidly start to expand and generates a high-frequency strain wave. The back interface, in the same time, reaches a lattice temperature of just over 400 K, and also generates a strain wave, but with a lower amplitude compared to the one generated at the surface.

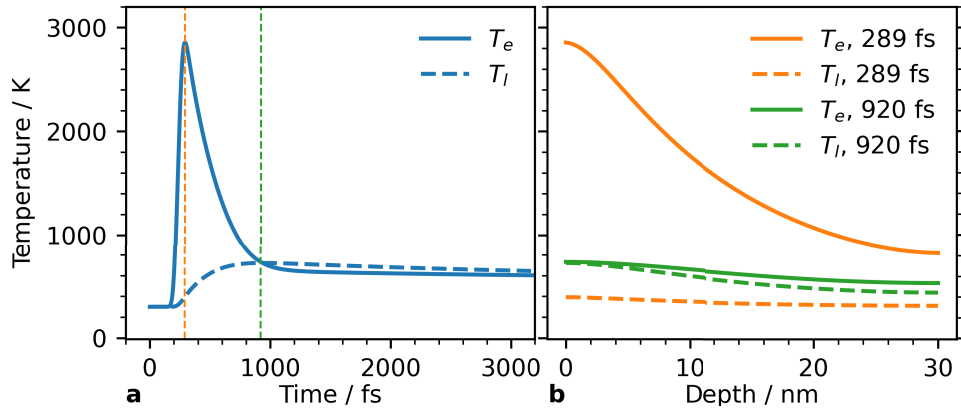


**Fig. 7.** a. Calculated electron (solid lines) and lattice (dashed lines) temperatures as function of time at the surface and, b. as a function of depth for  $t = 289$  fs and  $t = 920$  fs. The vertical dashed lines in a. indicate the peak of the electron temperature at  $t = 289$  fs (orange dashed line) and the moment the lattice and electron gas are in thermal equilibrium at the surface, at  $t = 920$  fs (green dashed line).

## B. Calculation of strain wave spectrum

Using the elastic wave equations [20], and using the lattice temperature calculated as a function of time and position from Appendix A, we calculate the displacement using a similar numerical model as in Ref. [20]. The 30 nm ruthenium film is considered to be free standing, i.e., at both front and back interface we consider a stress-free boundary condition. Material parameters for ruthenium are shown in Table 2.

**Table 2. Ruthenium material parameters used in the strain calculation. Values are taken from [33].**

Material parameter	Unit	Value
Young's modulus, $E$	GPa	447
Bulk modulus, $B$	GPa	220
Linear expansion coefficient, $\beta$	-	6.4e-4
Density, $\rho$	kg <sup>3</sup> m <sup>-1</sup>	12.37e3

Figure 8 shows, in the left column, the strain as a function of time at several positions along a line perpendicular to the surface. The average strain at each position in this time window has been subtracted. The solid lines show the calculated strain and the dashed lines show the strain multiplied by a Hann windowing function. Between 9 ps and 10 ps, depending on the position inside the layer, we see the strain wave returning to the surface. Up to 2 ps later, we see the strain wave propagating back into the layer, after being reflected off the surface. Before and after this main strain wave, we observe smaller peaks. These are caused by the strain wave that is generated at the back interface of the layer, and are mostly removed by the Hann window.

In the right column of Fig. 8, we see the corresponding strain-wave frequency spectra, obtained via FFT from the time-domain data shown in the left column. The strain wave is calculated using a time step of 40 as, but only saved at a sample rate of 10 fs.

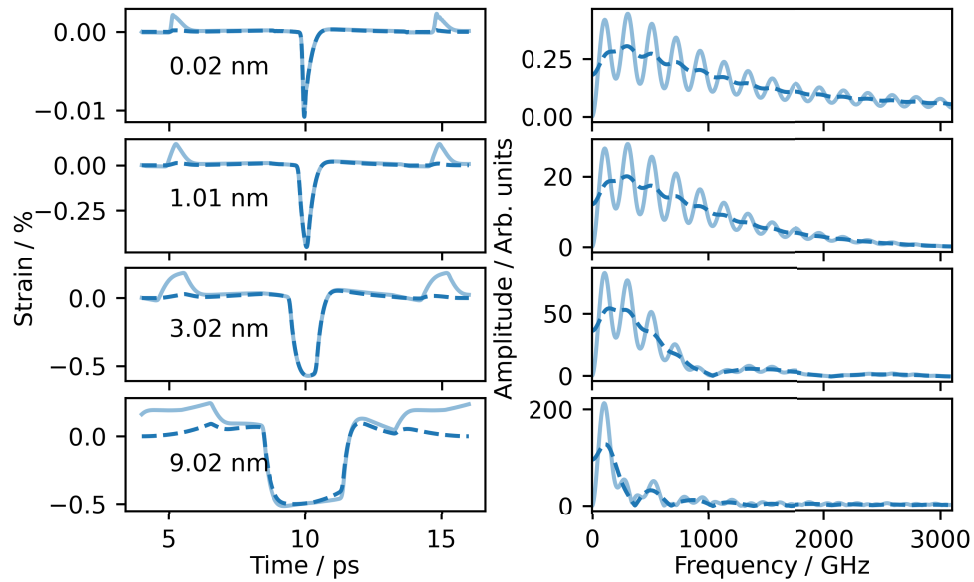


**Fig. 8.** Left column, calculated strain (solid lines) as a function of time at selected positions in the layer. Dashed lines: strain multiplied by a Hann window. Right column: amplitude of the FFT of the strain at selected positions. The solid line is the calculated strain, and dashed line is the Hann-windowed strain.

### C. FFT full time interval

The FFT of the 35 ps interval is shown in Fig. 9. It largely resembles the spectrum of the first echo (Fig. 2), but is modulated by 100 GHz, due to the 10 ps roundtrip time. Nonetheless, frequency components up to 600 GHz are still visible for probe wavelengths around 650 nm.

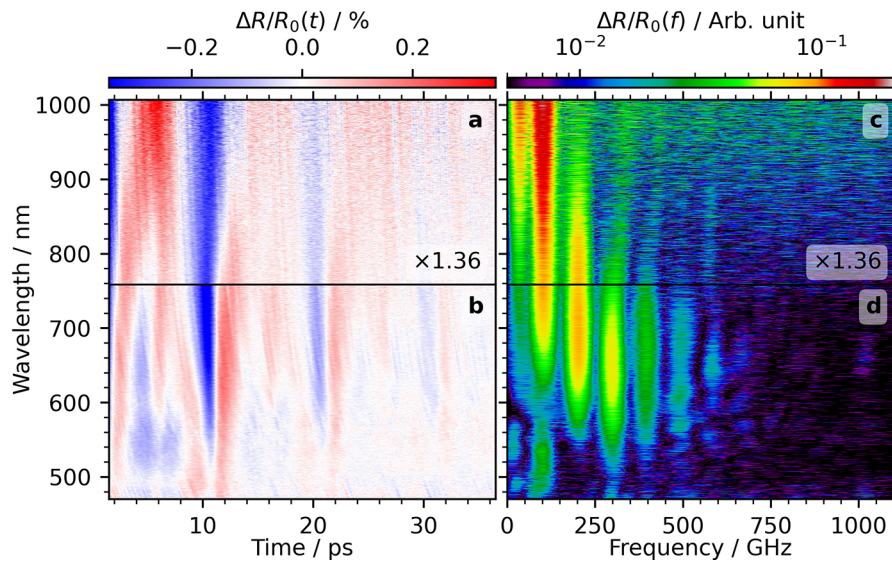


**Fig. 9.** a and b: Measured strain-wave-induced changes in reflectance of a 30 nm thick layer of ruthenium on sapphire, after removing the thermal background, identical to Fig. 2(a) and (b). c and d: FFT amplitudes of the 35 ps time interval shown in a and b. The amplitudes in a and c are multiplied by a factor of 1.36, see Appendix C.

#### D. Scaling of the longer-wavelength measurements

There is a distinct difference in the amplitude of the changes in reflectance between the short-wavelength measurement, for wavelengths between 408 nm and 760 nm, and the long-wavelength measurement, between 730 nm and 1000 nm. By scaling the latter by a factor of 1.36, the measurements overlap, as can be seen in Fig. 10(a) and (b). In Fig. 10(a), the change in reflectance, including thermal background, is shown for a probe wavelength of 740 nm from the short- and long-wavelength, in blue and orange, respectively. Figure 10(b), shows the background-removed changes in reflectance, induced by the strain wave, for probe wavelengths of 730 nm, 740 nm and 750 nm. The short-wavelength measurement is shown in blue and the long-wavelength measurement is shown in orange. The differences between the two sets of measurements are, after the adjustments, very small.

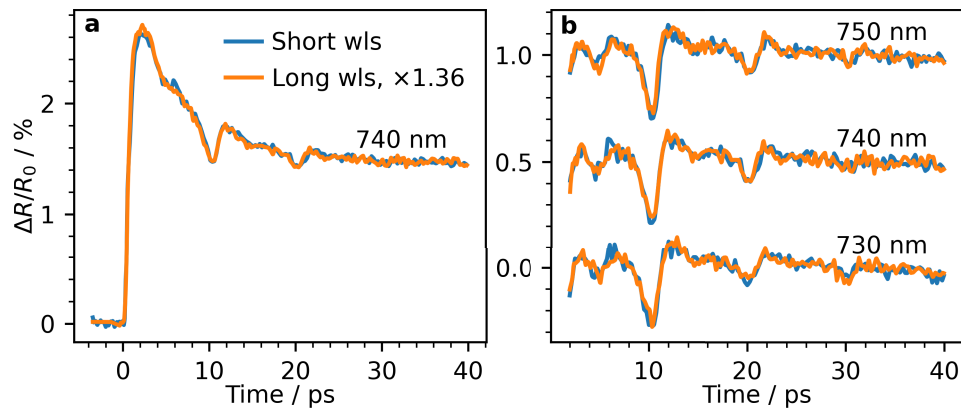


**Fig. 10.** a. Comparison between the change in reflectance measured at 740 nm from the short-wavelength measurement (blue) and measured at the same wavelength from the long-wavelength measurement (orange), that is scaled by 1.36. b. Comparison between the strain-wave-induced reflectance changes at 730 nm, 740 nm, and 750 nm from the short- (blue) and long-wavelength (orange) measurement. The data from the long-wavelength measurement is scaled by 1.36, again. The curves are offset for visibility.

**Acknowledgment.** This work was conducted at the Advanced Research Center for Nanolithography, a public-private partnership between the University of Amsterdam, Vrije Universiteit Amsterdam, University of Groningen, the Netherlands Organization for Scientific Research (NWO), and the semiconductor equipment manufacturer ASML.

**Disclosures.** The authors declare no conflicts of interest.

**Data availability.** Data underlying the results presented in this paper are not publicly available at this time but may be obtained from the authors upon reasonable request.

#### References

1. P. Kapur, J. McVittie, and K. Saraswat, "Technology and reliability constrained future copper interconnects. I. Resistance modeling," *IEEE Trans. Electron Devices* **49**(4), 590–597 (2002).
2. S. Paolillo, D. Wan, F. Lazzarino, *et al.*, "Direct metal etch of ruthenium for advanced interconnect," *J. Vac. Sci. & Technol. B, Nanotechnol. Microelectron. Materials, Process. Meas. Phenom.* **36**(3), 03E103 (2018).
3. D. Gall, "The search for the most conductive metal for narrow interconnect lines," *J. Appl. Phys.* **127**(5), 050901 (2020).
4. L. G. Wen, P. Roussel, O. V. Pedreira, *et al.*, "Atomic Layer Deposition of Ruthenium with TiN Interface for Sub-10 nm Advanced Interconnects beyond Copper," *ACS Appl. Mater. Interfaces* **8**(39), 26119–26125 (2016).
5. W. J. Mitchell, B. J. Thibeault, D. D. John, *et al.*, "Highly selective and vertical etch of silicon dioxide using ruthenium films as an etch mask," *J. Vac. Sci. & Technol. A: Vacuum, Surfaces, Films* **39**(4), 043204 (2021).
6. Z. Chen, A. Ranjan, and P. Ventzek, "Ruthenium Hard Mask Process," (2020).
7. Y.-T. Lu, K.-H. Yu, and A. Raley, "Method for using ultra thin ruthenium metal hard mask for etching profile control," (2021).

8. A. J. den Boef, "Optical wafer metrology sensors for process-robust CD and overlay control in semiconductor device manufacturing," *Surf. Topogr.: Metrol. Prop.* **4**(2), 023001 (2016).
9. S. Edward, H. Zhang, I. Setija, *et al.*, "Detection of Hidden Gratings through Multilayer Nanostructures Using Light and Sound," *Phys. Rev. Appl.* **14**(1), 014015 (2020).
10. V. Verrina, S. Edward, H. Zhang, *et al.*, "Photoacoustic detection of low duty cycle gratings through optically opaque layers," *Appl. Phys. Lett.* **117**(5), 051104 (2020).
11. G. de Haan, V. Verrina, A. J. L. Adam, *et al.*, "Plasmonic enhancement of photoacoustic-induced reflection changes," *Appl. Opt.* **60**(24), 7304 (2021).
12. T. J. van den Hooven and P. C. M. Planken, "Surface-plasmon-enhanced strain-wave-induced optical diffraction changes from a segmented grating," *Photoacoustics* **31**, 100497 (2023).
13. T. J. van den Hooven and P. C. M. Planken, "Wavelength-Dependent Optical Detection of Strain Waves near Intrinsic and Artificial Optical Resonances," *Opt. Lett.* **50**(5), 1445–1448 (2025).
14. F. Noll, N. Krauß, V. Gusev, *et al.*, "Surface plasmon-based detection for picosecond ultrasonics in planar gold-dielectric layer geometries," *Photoacoustics* **30**, 100464 (2023).
15. K. Chaudhary, M. Illienko, T. J. van den Hooven, *et al.*, "Optically enhancing and controlling photoacoustic signals using ultra-thin semiconductor coatings on metal surfaces," *Opt. Express* **33**(1), 199 (2025).
16. F. Akhmetov, I. Milov, S. Semin, *et al.*, "Laser-induced electron dynamics and surface modification in ruthenium thin films," *Vacuum* **212**, 112045 (2023).
17. F. Akhmetov, J. Vorberger, I. Milov, *et al.*, "Ab initio-simulated optical response of hot electrons in gold and ruthenium," *Opt. Express* **32**(11), 19117 (2024).
18. L. Cruciani, S. Van Vliet, A. Troglia, *et al.*, "Femtosecond Laser-Induced Emission of Coherent Terahertz Pulses from Ruthenium Thin Films," *J. Phys. Chem. C* pp. 1932–7447 (2023).
19. L. Cruciani, M. Vreugdenhil, S. Van Vliet, *et al.*, "Direct laser patterning of ruthenium below the optical diffraction limit," *Appl. Phys. Lett.* **124**(17), 171902 (2024).
20. G. de Haan, T. J. van den Hooven, and P. C. M. Planken, "Ultrafast laser-induced strain waves in thin ruthenium layers," *Opt. Express* **29**(20), 32051 (2021).
21. A. Dubietis, G. Tamošauskas, R. Šūminas, *et al.*, "Ultrafast supercontinuum generation in bulk condensed media," *Lith. J. Phys.* **57**(3), 1 (2017).
22. F. Akhmetov, I. Milov, I. A. Makhotkin, *et al.*, "Electron-phonon coupling in transition metals beyond Wang's approximation," *Phys. Rev. B* **108**(21), 214301 (2023).
23. Y. Petrov, K. Migdal, N. Inogamov, *et al.*, "Ruthenium under ultrafast laser excitation: Model and dataset for equation of state, conductivity, and electron-ion coupling," *Data in Brief* **28**, 104980 (2020).
24. G. V. Samsonov, *Handbook of the Physicochemical Properties of the Elements* (Springer, New York, NY, 1968).
25. P. Babilotte, P. Ruello, D. Mounier, *et al.*, "Femtosecond laser generation and detection of high-frequency acoustic phonons in GaAs semiconductors," *Phys. Rev. B* **81**(24), 245207 (2010).
26. O. Matsuda, T. Pezeril, I. Chaban, *et al.*, "Time-domain Brillouin scattering assisted by diffraction gratings," *Phys. Rev. B* **97**(6), 064301 (2018).
27. E. D. Palik, *Handbook of Optical Constants of Solids* (Elsevier professional, s.l., 1997), 1st ed.
28. M. Illienko, M. C. Velsink, and S. Witte, "Understanding photoacoustic signal formation in the presence of transparent thin films," *Photoacoustics* **38**, 100617 (2024).
29. C. He, O. Ristow, M. Grossmann, *et al.*, "Acoustic waves undetectable by transient reflectivity measurements," *Phys. Rev. B* **95**(18), 184302 (2017).
30. S. Anisimov, B. Kapeliovich, and T. Perel'man, "Electron emission from the metal surfaces induced by ultrashort lasers pulses," *Zhurnal Eksperimental'noj i Teoreticheskoy Fiziki* **66**, 776–781 (1974).
31. M. Bonn, D. N. Denzler, S. Funk, *et al.*, "Ultrafast electron dynamics at metal surfaces: Competition between electron-phonon coupling and hot-electron transport," *Phys. Rev. B* **61**(2), 1101–1105 (2000).
32. S. J. Byrnes, "Multilayer optical calculations," (2020).
33. "ElementData Source Information—Wolfram Language Documentation," <https://reference.wolfram.com/language/note/ElementDataSourceInformation.html>.